# A novel approach to tracer-kinetic modeling for (macromolecular) dynamic contrast-enhanced MRI

# A Novel Approach to Tracer-Kinetic Modeling for (Macromolecular) Dynamic Contrast-Enhanced MRI

Igor Jacobs,[1]* Gustav J. Strijkers,[1,2] Henk M. Keizer,[3] Henk M. Janssen,[3] Klaas Nicolay,[1] and Matthias C Schabel[4,5]

**Purpose:** To develop a novel tracer-kinetic modeling approach for multi-agent dynamic contrast-enhanced MRI (DCE-MRI) that facilitates separate estimation of parameters characterizing blood flow and microvascular permeability within one individual.
**Methods:** Monte Carlo simulations were performed to investigate the performance of the constrained multi-agent model. Subsequently, multi-agent DCE-MRI was performed on tumor-bearing mice (n = 5) on a 7T Bruker scanner on three measurement days, in which two dendrimer-based contrast agents having high and intermediate molecular weight, respectively, along with gadoterate meglumine, were sequentially injected within one imaging session. Multi-agent data were simultaneously fit with the gamma capillary transit time model. Blood flow, mean capillary transit time, and bolus arrival time were constrained to be identical between the boluses, while extraction fractions and washout rate constants were separately determined for each agent.
**Results:** Simulations showed that constrained multi-agent model regressions led to less uncertainty and bias in estimated tracer-kinetic parameters compared with single-bolus modeling. The approach was successfully applied in vivo, and significant differences in the extraction fraction and washout rate constant between the agents, dependent on their molecular weight, were consistently observed.
**Conclusion:** A novel multi-agent tracer-kinetic modeling approach that enforces self-consistency of model parameters and can robustly characterize tumor vascular status was demonstrated. **Magn Reson Med 75:1142–1153, 2016. © 2015 Wiley Periodicals, Inc.**

**Key words:** dynamic contrast-enhanced MRI; macromolecular contrast agents; tracer-kinetic modeling; perfusion and permeability; tumor vasculature; cancer imaging

## INTRODUCTION

Accurate evaluation of antivascular tumor therapy requires a detailed assessment of the induced vascular changes (1). Dynamic contrast-enhanced MRI (DCE-MRI) has been widely employed for characterization of tumor microvasculature (2) and evaluation of antivascular therapies (3–5). Tracer-kinetic modeling of DCE-MRI data can be applied to identify vascular biomarkers that could be used for accurate treatment assessment and optimization (6–8). The most commonly applied pharmacokinetic models that have been used in the evaluation of antivascular tumor therapies are the standard and extended Tofts models (9,10). One of the parameters that can be determined with these models is the transfer constant $K^{trans}$, which is influenced by tumor blood flow, microvascular surface area, and capillary permeability (11). In many of the clinical trials of antivascular agents in which DCE-MRI has been used for treatment evaluation, a reduction in $K^{trans}$ has been reported as evidence for drug efficacy (5–7). This reduction may be associated with a decrease in blood flow and/or microvascular permeability, but these parameters cannot be separately resolved because the interpretation of $K^{trans}$ is dependent on the perfusion regime of the tumor (11). Separate determination of blood flow and microvascular permeability would be of great value. Vascular targeting agents, aimed at destruction of the existing tumor vasculature, can induce an early increase in microvascular permeability and subsequent reduction in blood flow, having counteracting effects on $K^{trans}$ (12,13). Furthermore, antiangiogenic therapy may induce (transient) blood vessel normalization, resulting in alterations in multiple vascular parameters (14,15). The ability to noninvasively identify the different vascular alterations induced by antivascular therapy may provide an improved understanding of the mechanisms of drug action and aid in accurate assessment and optimization of antivascular therapies.

Different strategies have been suggested to improve the precision with which these vascular alterations may be characterized. More advanced tracer-kinetic models have been developed that facilitate separate assessment of blood flow, capillary transit time, vascular heterogeneity, microvascular permeability, and blood volume (16–18). However, application of these models is limited due to the more stringent requirements on data acquisition (18–20). It has been proposed that the use of macromolecular contrast agents may facilitate better assessment of specific tracer-kinetic parameters; low molecular weight contrast agents have high transendothelial diffusion and are therefore more sensitive to blood flow changes,

[1]Biomedical NMR, Department of Biomedical Engineering, Eindhoven University of Technology, Eindhoven, Netherlands.
[2]Biomedical Engineering and Physics, Academic Medical Center, University of Amsterdam, Amsterdam, Netherlands.
[3]SyMO-Chem BV, Eindhoven, Netherlands.
[4]Advanced Imaging Research Center, Oregon Health & Science University, Portland, Oregon, USA.
[5]Utah Center for Advanced Imaging Research, University of Utah, Salt Lake City, Utah, USA.
*Correspondence to: Igor Jacobs, M.Sc., Biomedical NMR, Department of Biomedical Engineering, Eindhoven University of Technology, High Tech Campus 11, Office 1.245, P.O. Box 513, 5600 MB Eindhoven, Netherlands. E-mail: i.jacobs@tue.nl

This research was performed within the framework of CTMM, the Center for Translational Molecular Medicine (www.ctmm.nl), project VOLTA (grant 05T-201).
Received 29 October 2014; revised 26 February 2015; accepted 26 February 2015
DOI 10.1002/mrm.25704
Published online 4 April 2015 in Wiley Online Library (wileyonlinelibrary.com).

whereas the limited transendothelial diffusion and long intravascular half-life of macromolecular agents make them more sensitive to permeability and blood volume changes (21,22). Several studies have shown that combining low molecular weight contrast agents with macromolecular contrast agents can facilitate improved assessment of tracer-kinetic parameters and changes therein after treatment (23–28). In most of these studies, DCE-MRI with the various contrast agents was performed in separate animals or at different experimental time points, whereas others have shown that contrast agents of various molecular weight can be combined in one imaging protocol (29–33). In these studies, often the different boluses were separately analyzed, and accurate assessment of the diverse vascular changes induced by antivascular therapies could benefit from modeling contrast agent uptake in more detail.

Therefore, the aim of the present study was to develop a novel tracer-kinetic modeling approach that facilitates separate estimation of the parameters characterizing blood flow and microvascular permeability within one individual. A multi-agent DCE-MRI approach was developed in which contrast agents of various molecular weights were sequentially injected under identical circumstances within one imaging session (34). A novel tracer-kinetic modeling strategy for multi-agent DCE-MRI was developed in which a number of tracer-kinetic parameters were constrained to be identical between the different agents based on physiological grounds, while other parameters were separately determined for each contrast agent bolus. The performance of the multi-agent tracer-kinetic modeling approach was demonstrated with simulations, and the method was applied in vivo in a mouse tumor model. It is hypothesized that this approach, based on simultaneous fitting of the multi-agent data, is suitable to robustly assess the tumor vascular status, and it is expected that the presented method can be applied to accurately evaluate treatment effects on different vascular biomarkers.

## METHODS

### Tracer-Kinetic Modeling

Our multi-agent tracer-kinetic modeling approach was based on the gamma capillary transit time (GCTT) model (35). This model can be expressed as:

$$C_t(t) = F(R_v(t) + R_p(t)) \star C_a(t). \quad [1]$$

where $C_t(t)$ is the measured total tissue contrast agent concentration, $R_v(t)$ is the vascular impulse response function, $R_p(t)$ is the parenchymal impulse response function, $C_a(t)$ is the contrast agent concentration in the arterial blood, and F is the blood flow. The asterisk represents the convolution operator.

For the GCTT model, the vascular and parenchymal impulse response functions are described by the following equations:

$$R_v(t) = 1 - \int_0^t D(u)du. \quad [2]$$

$$R_p(t) = E \int_0^t D(u)e^{-k_{ep}(t-u)}du, \quad [3]$$

where D(u) is the distribution of capillary transit times, E is the extraction fraction, and $k_{ep}$ is the washout rate constant. In the GCTT model, the transit time distribution is described by a gamma distribution on the mean capillary transit time ($t_c$) and capillary transit time heterogeneity ($\sigma_c$):

$$D(t; t_c, \sigma_c) = \frac{t^{\alpha-1}e^{-t/\tau}}{\tau^{\alpha}\Gamma(\alpha)}, \quad [4]$$

where $\alpha = \sqrt{t_c/\sigma_c}$, $\tau = \sigma_c^2/t_c$, and $\Gamma(\alpha)$ is the gamma-variate function.

Therefore, the GCTT model can be fully specified by a total of six parameters: the blood flow F ($min^{-1}$), extraction fraction E, washout rate constant $k_{ep}$ ($min^{-1}$), mean capillary transit time $t_c$ (min), vascular heterogeneity index $\alpha^{-1}$, and a delay time $t_d$ (min) between contrast agent injection and bolus arrival in the tumor. A number of tracer-kinetic parameters can be derived from this model: the transfer constant $K^{trans} = E * F$ ($min^{-1}$), extravascular extracellular volume fraction $v_e = E * F/k_{ep}$, and fractional blood volume $v_b = F * t_c$. The Renkin–Crone equation can then be used to estimate the permeability surface area product $PS = -F * \log(1 - E)$ ($min^{-1}$) (36,37).

### Constrained Multi-agent Tracer-Kinetic Modeling

The multi-agent modeling approach is based on the assumption that a number of tracer-kinetic parameters can be constrained to be identical between the different boluses based on physiological grounds. For N different contrast agent boluses, the unconstrained GCTT model is defined by a total number of 6N free parameters. However, the cardiac output and tumor hemodynamics are relatively constant over the time-scale of the multi-agent DCE-MRI experiment and therefore the blood flow, mean capillary transit time, capillary transit time dispersion, and delay time are not expected to be significantly different between the different contrast agent boluses. When these parameters are constrained to be identical between the sequentially injected boluses, the number of free parameters in the multi-agent modeling is reduced to $6 + 2(N - 1)$. Only the extraction fractions and washout rate constants (which are dependent on the molecular dimensions of the contrast agents) are now varied between the different contrast agent boluses. Initial modeling revealed large uncertainty in estimates of the vascular heterogeneity index ($\alpha^{-1}$) for these data, so this parameter was fixed to a value of 1, which is appropriate for tumor tissues where vascular heterogeneity is known to be large, as is typical in malignant tumors (38).

### Bootstrapping Initialization of the Nonlinear Optimization Algorithm

Bootstrapping initialization was applied to minimize the chance of becoming trapped in a local minimum during model regression; initial parameter values for the

extended Tofts model were determined by using a fast linearized tracer-kinetic modeling algorithm. The limiting mathematical relationship between the extended Tofts model and GCTT model for $lim_{t_c \to 1}$ and $lim_{\sigma_c \to 0}$ was then used to obtain initial parameter estimates for the GCTT model. Subsequently, nonlinear regression was performed separately for each bolus injection by sequential fitting of the individual boluses using the "lsqcurvefit" function in MATLAB (MathWorks, Natick, Massachusetts, USA). Constrained parameters were then initialized by taking the median of the estimates obtained from the separate fits of the different injections. Unconstrained parameters were directly initialized from the unconstrained regressions. All parameters were constrained to be positive in the model regressions.

### Simulations

Monte Carlo simulations were performed to investigate the performance of the constrained multi-agent model. In vivo DCE-MRI data were acquired from a human glioblastoma patient with a temporal resolution of 3.2 s per frame and a standard bolus injection of a low molecular weight contrast agent (gadobenate dimeglumine, Multihance, 0.1 mmol/kg) (35,38). Precontrast $T_1$ values were determined with a variable flip angle approach (39). Measured signal changes were converted to contrast agent concentration (40), the arterial input function (AIF) was determined using a blind estimation algorithm (41,42), and the DCE-MRI data were fit with the GCTT model (35). Model parameters that were selected from a region of interest (ROI) placed in a relatively homogeneous, enhancing tumor region were averaged to obtain the following simulated tissue uptake curve parameters: $F = 0.256$ min$^{-1}$, $v_e = 0.570$, $t_c = 15.5$ s, and $\alpha^{-1} = 0.5$ ($v_b = 0.066$). A multi-agent experiment was subsequently simulated as follows: three contrast agent injections were simulated, starting with high molecular weight (HMW, $E = 0.05$), followed by medium molecular weight (MMW, $E = 0.27$) and finally low molecular weight (LMW, $E = 0.54$), determined as above from the measured data. Contrast agent injections were spaced by 6 min, with 30 s of baseline acquisition prior to injection of the first agent. Gaussian noise with a standard deviation of 0.04 mM (equal to the noise level in the original human study, which corresponds to a signal-to-noise ratio of approximately 7) was added to generate 1000 random realizations of the tissue contrast agent uptake curve. Each realization was fit with the constrained model, simultaneously fitting all three superimposed uptake curves. Individual uptake curves for each agent were also fit separately with the unconstrained model. Estimated model parameters were subsequently compared with the known starting values to determine the bias and uncertainty in the estimated parameters for both the constrained and the unconstrained modeling approach.

### Contrast Agents for In Vivo Multi-agent DCE-MRI

Multi-agent experiments in tumor-bearing mice were performed with contrast agents with a range of molecular weights but an equal composition. Modified poly(propylene imine) (PPI) dendrimers, functionalized with Gd-DOTA moieties through a polyethylene glycol (PEG) spacer (Fig. 1), were synthesized by SyMO-Chem BV (Eindhoven, Netherlands). An intermediate molecular weight dendrimer of generation 2 [G2-PPI-(PEG$_6$-GdDOTA)$_8$], high molecular weight dendrimer of generation 5 [G5-PPI-(PEG$_6$-GdDOTA)$_{64}$], and low molecular weight agent gadoterate meglumine (Gd-DOTA, Dotarem, Guerbet, Villepente, France) were used in the in vivo multi-agent experiments. Synthesis of the dendrimers according to their theoretical structure was confirmed using $^1$H-NMR (prior to Gd complexation). Additional information on synthesis and further characterization of the dendrimers (after Gd complexation), including gel permeation chromatography, dynamic light scattering, and inductively coupled plasma-atomic emission spectrometry, is given in Supporting Information 1. The molecular weight, diameter, and plasma relaxivity measured at 7T at 37°C of the contrast agents are listed in Table 1. For the in vivo multi-agent experiments, an infusion line was filled with equal volumes of the generation 5 (G5) and generation 2 (G2) dendrimer and gadoterate meglumine (at a concentration of 125 mM Gd, ~0.1 mmol Gd/kg), separated by equal volumes of saline. A small air bubble between all volumes prevented mixing of the different solutions.

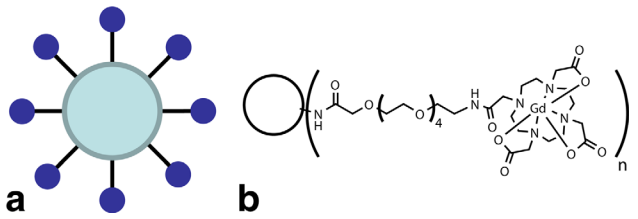


FIG. 1. Representation of the dendrimer-based contrast agents. **A:** Schematic drawing of the G2 dendrimer, in which the dendrimer core is represented by the large circle, to which multiple Gd-DOTA moieties (blue circles) are attached via a PEG-spacer (black lines). **B:** General dendrimer structure, consisting of a dendrimer core (represented by the large circle) and a variable number (n) Gd-DOTA moieties attached via the PEG linkers, dependent on the dendrimer generation.

### Ethics Statement

All animal experiments were performed according to Directive 2010/63/EU of the European Commission and were approved by the Animal Care and Use Committee of Maastricht University (Protocol 2010-132).

### Animal Model

CT26.WT murine colon carcinoma cells (American Type Culture Collection [ATCC; CRL-2638]) were cultured as a monolayer at 37°C and 5% $CO_2$ in RPMI-1640 medium (Invitrogen, Breda, Netherlands) supplemented with 10% fetal bovine serum (Greiner Bio-One, Alphen a/d Rijn, Netherlands) and 50 U/mL penicillin/streptomycin (Lonza Bioscience, Basel, Switzerland). Early passages (5–10) of the original ATCC batch were used for inoculation.

10- to 12-week-old Balb/c mice (Charles River, Maastricht, Netherlands) were inoculated with $1 \times 10^6$

Table 1
General Characteristics of the Different Contrast Agents

| Contrast agent | Molecular Weight (Da) | Diameter (nm) | $r_1$ ($mM^{-1} * s^{-1}$) | $r_2$ ($mM^{-1} * s^{-1}$) | $r_2/r_1$ |
|---|---|---|---|---|---|
| Gadoterate meglumine | 754 | 0.9[a] | 3.6 | 4.0 | 1.12 |
| G2-PPI-$(PEG_6$-GdDOTA$)_8$ | 7317 | $4.3 \pm 1.1$ | 5.5 | 6.6 | 1.19 |
| G5-PPI-$(PEG_6$-GdDOTA$)_{64}$ | 59517 | $10.0 \pm 3.6$ | 7.2 | 10.0 | 1.39 |

The molecular weight is the theoretical molecular weight of the different contrast agents. The hydrodynamic diameter and distribution widths of the dendrimers were determined in PBS of pH 7.4 (Supporting Information 1).
[a]The diameter of gadoterate meglumine was obtained from Corot et al. (61). The longitudinal ($r_1$) and transverse ($r_2$) relaxivities of the agents were measured in Balb/c mouse plasma at 7T at 37°C.

CT26.WT cells subcutaneously in the right hind limb. Approximately 10 days after inoculation, tumors became palpable in all animals.

### In Vivo Multi-agent DCE-MRI in Tumor-Bearing Mice

Multi-agent DCE-MRI experiments were performed on a 7T Bruker BioSpec 70/30 USR equipped with a 1H 59/35 (outer/inner diameter in mm) circular polarized MRI transceiver volume coil. All mice underwent MRI three times with 2 days of recovery in between to investigate whether differences in extraction fraction and washout rate constant between the agents can consistently be observed. For the MRI measurements, mice were anesthetized with isoflurane (3% for induction, 1%–2% for maintenance) in medical air (flow rate of 0.4 L/min). During the measurements, mice were positioned in a custom-made cradle, equipped with a mask for anesthetic gas. Respiration rate was monitored with a balloon sensor, and body temperature was monitored and maintained with a warm water pad. To minimize susceptibility artifacts at air–tissue interfaces, the tumor was covered with a small layer of degassed ultrasound gel (Aquasonic 100; Parker Laboratories, Fairfield, New Jersey, USA), and artifacts were further reduced by local shimming of the tumor-bearing paw.

A three-dimensional $T_2$-weighted (effective echo time [TE] = 34 ms) turbo rapid acquisition with relaxation enhancement (RARE) acquisition was performed for anatomical reference. $B_1$ mapping was performed based on the 180° signal-null method (43). Precontrast $T_1$ mapping was performed using a variable flip angle gradient-spoiled (5 ms duration) and radiofrequency-spoiled three-dimensional fast low-angle shot sequence using the following sequence parameters: repetition time (TR) = 20 ms; TE = 3.23 ms; acquisition matrix = 52 × 72 × 14 (reconstructed to 96 × 96 × 16); field of view = 30 × 30 × 24 $mm^3$; and flip angle = 2°, 3°, 5°, 7°, 10°, 13°, 20° (39,44,45). $T_1$ values were determined using a DESPOT1 (driven equilibrium single-pulse observation of $T_1$) analysis (39). For the multi-agent DCE-MRI measurements, a gradient-spoiled (5 ms duration) and radiofrequency-spoiled three-dimensional fast low-angle shot sequence (covering the tumor) was applied using the following sequence parameters: TR = 2.5 ms; TE = 0.84 ms; flip angle = 6°; acquisition matrix = 52 × 72 × 14 (reconstructed to 96 × 96 × 16); field of view = 30 × 30 × 24 $mm^3$; temporal resolution = 1.89 s; and total scan time = 47 min. Phantom measurements for validation of the variable flip angle and dynamic $T_1$ mapping method are shown in Supporting Information 2. Contrast injections were performed at 2 (G5 dendrimer), 17 (G2 dendrimer), and 32 (gadoterate meglumine) min after the start of the acquisition, using an infusion pump (Chemyx Fusion 100, Stafford, Texas, USA) at a rate of 2 mL/min. $B_1$-corrected $\Delta R_1$ ($=1/\Delta T_1$) values were calculated on a pixel-by-pixel basis based on the standard signal equation for a spoiled gradient echo sequence (40) using the precontrast $T_1$ values and the postcontrast dynamic signal intensities. Regions of interest delineating the tumor tissue were manually drawn on the anatomic images.

### In Vivo Multi-agent Modeling

AIFs composed of one bolus for each of the three injected agents were determined for each agent separately using the Monte Carlo Blind Estimation (MCBE) algorithm applied to the $\Delta R_1$ curves of enhancing tumor voxels (41,42). Each individual bolus within the AIF was modeled by a gamma-variate function with recirculation and a sigmoid representing contrast at quasi-equilibrium in the blood pool (41). During the blind AIF estimation, tissue curves were modeled using the GCTT model with vascular heterogeneity index ($\alpha^{-1}$) fixed to a value of 1. The algorithm was initialized using a population averaged AIF from previous measurements made in the left ventricular lumen of mice that were injected with gadopentetic acid with a similar injection protocol (46). MCBE estimation of the AIF of the first injected agent (G5 dendrimer) was performed by truncating the tissue curves before injection of the second agent (G2 dendrimer). The resulting AIF for the G5 dendrimer bolus was then used to generate model curve fits to the tissue curves, and these fits were subtracted from the measured tissue data to remove the effect of uptake of G5 dendrimer. This procedure was then repeated for the G2 dendrimer and gadoterate meglumine injections to provide separate AIF estimates for each agent. Differences in relaxivities between the different agents were compensated by rescaling each bolus to an equivalent dose of gadoterate meglumine using measured relaxivities for the different agents. Exemplary AIFs of the dendrimers and gadoterate, as determined with the MCBE algorithm, are shown in Supporting Information 3. The tracer-kinetic model described by Equation [1] is invariant under the simultaneous transformation $C_p\ (t) \rightarrow \gamma C_p\ (t)$, $F \rightarrow F/\gamma$ and $v_b \rightarrow v_b/\gamma$ for any scalar value of $\gamma$ (41). Therefore, the global AIF scale factor $\gamma$ remains indeterminate, as is common for blind AIF estimation methods. This scale factor could be obtained from a secondary reference measurement of the true contrast agent concentration in the blood, which has not been employed in the present

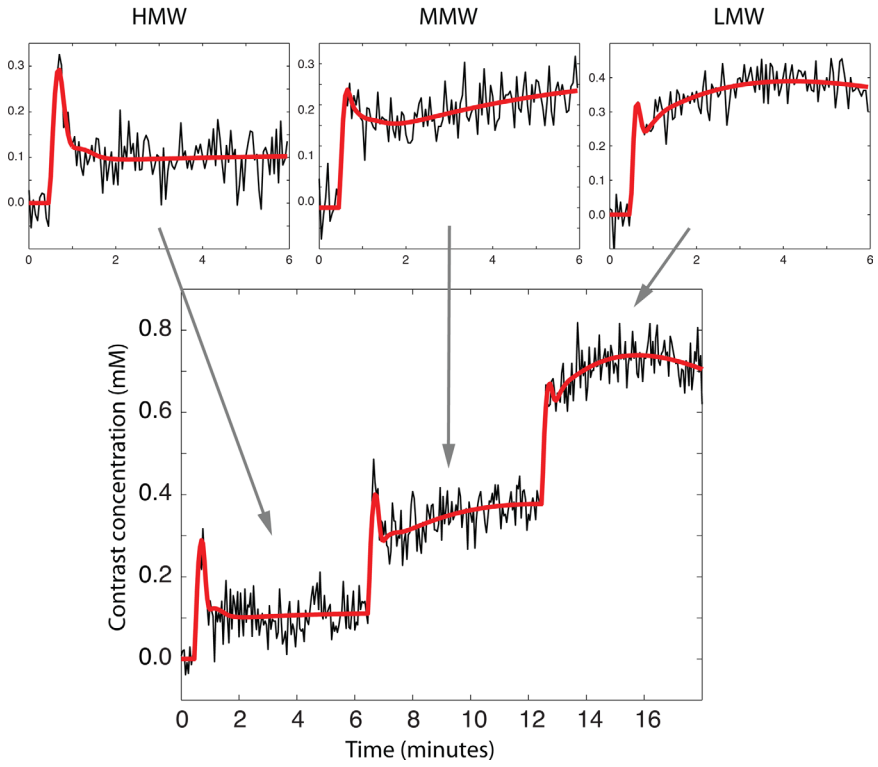


FIG. 2. Unconstrained and constrained regressions to simulated data. Simulated data for LMW, MMW, and HMW contrast media (black curves). Regressions to simulated data are shown by the red curves. Data in the top three panels are fit separately with the unconstrained model; in the bottom panel, all data are simultaneously fit.

study. As a result, absolute values for F and $v_b$ could not be derived, and these parameter estimates are scaled by the amplitude of the initial population-averaged AIF provided to the MCBE algorithm as a starting guess.

Multi-agent data were simultaneously fit with the GCTT model with vascular heterogeneity index ($\alpha^{-1}$) fixed to a value of 1. Blood flow (F), mean capillary transit time ($t_c$), and bolus arrival time ($t_d$) were constrained to be identical between the different boluses, while extraction fractions (E) and washout rate constants ($k_{ep}$) were separately determined for each contrast agent. Blood volume fractions ($v_b$) were calculated by F * $t_c$. Median pharmacokinetic parameters were calculated in all tumor pixels with statistically significant blood flow and low uncertainty in blood flow, relative to the estimated blood flow value. Median tumor parameter values for each measurement day were determined by taking the median of the median parameter values of all perfused tumor pixels of all mice.

### Statistics

Data are reported as median ± median absolute deviation of the five mice for each measurement day. Differences in the perfused tumor fraction and the constrained tracer-kinetic parameters blood flow and mean capillary transit time between the different measurement days were statistically analyzed using repeated-measures analysis of variance. Differences in the tracer-kinetic parameters extraction fraction and washout rate constant between measurement days and between the different contrast agents were analyzed using mixed-model repeated-measures analysis of variance with a post hoc Games–Howell test, with the time point as the within-subjects factor and the contrast agent as the between subject factor. The level of statistical significance was set at $\alpha = 0.05$.

## RESULTS

### Simulations

Simulated data for LMW, MMW, and HMW contrast agents are shown in Figure 2. Regressions with the unconstrained model are shown in the upper three panels, and the constrained multi-agent regressions are shown in the bottom panel. The simulated data demonstrate differences in the enhancement pattern, dependent on the molecular weight of the contrast agents, and the multi-agent regressions are observed to fit the simulated data well. Box plots of the results from the Monte Carlo simulations of the multi-agent and single-bolus modeling are shown in Figure 3, in which the estimated model parameters are compared with the known true parameter values. The median parameter estimates from the multi-agent modeling were consistently closer to the true parameter values compared with the single-bolus modeling approach. In addition, the bias and uncertainty in estimated tracer-kinetic parameters were consistently lower for the multi-agent data than for the single-bolus data. With the exception of $v_e$, the LMW contrast agent data were associated with the largest bias and uncertainty in the estimated tracer-kinetic parameters.

### In Vivo Multi-agent Measurements and Modeling

Contrast enhancement in the tumor after injection of the different contrast agents is shown in Figure 4. An increase in signal intensity could be observed 1 min after injection of the G5 dendrimer (1 min post G5), especially

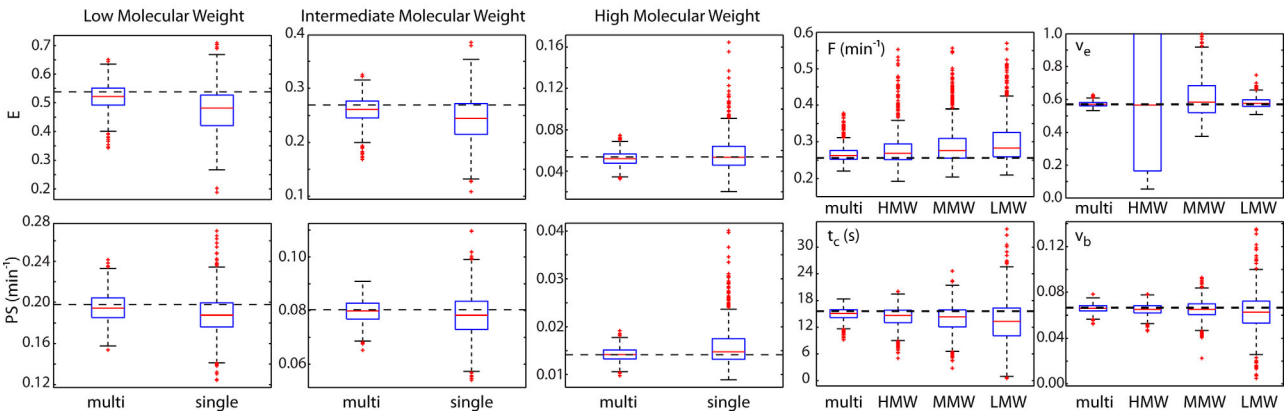


FIG. 3. Monte Carlo multi-agent simulation results. Box plots showing results for Monte Carlo simulation of 1000 noise realizations. True parameter values are indicated by horizontal dashed lines (black) and median estimates are indicated by red lines, with the 25$^{th}$ and 75$^{th}$ percentiles indicated by blue boxes. Outliers are plotted with red crosses. The three left-most columns show E and PS for the three different molecular weights, with the multi-agent model estimates on the left of each panel and the single bolus estimates on the right. The two right-most columns show the constrained parameter estimates, with the multi-agent estimates on the left, followed by the HMW, MMW, and LMW estimates.

in the well-vascularized tumor rim. In addition, some enhancement was visible in the tumor center. After injection of the G2 dendrimer (1 min post G2), a further increase in signal intensity was visible in most of the tumor area. Injection of gadoterate (1 min post gadoterate) resulted in further contrast enhancement, with a diffuse enhancement pattern throughout the tumor tissue. A small tumor region was characterized by an apparent lack of contrast enhancement.

Representative multi-agent DCE curves, measured in single pixels in different locations within the tumor, are depicted in Figure 5. Figure 5A shows the multi-agent data from a single pixel in the tumor rim. A pronounced increase in $\Delta R_1$ could be observed upon injection of the different contrast agents. Enhancement curves were well-defined, and a distinct enhancement pattern was visible after injection of the different agents. Contrast enhancement after injection of the G5 dendrimer was characterized by a step-wise increase in $\Delta R_1$, after which the $\Delta R_1$ remained relatively constant. A less steep upslope and a more pronounced washout phase were observed after injection of the G2 dendrimer. After injection of gadoterate, a rapid increase in $\Delta R_1$ was followed by a rapid decrease afterward due to contrast agent washout. These differences in enhancement pattern were reflected by the different pharmacokinetic parameter estimates for the different agents (Fig. 5). Figure 5B shows representative data from a pixel in the tumor center. Whereas contrast enhancement was generally lower in this pixel, similar differences in enhancement pattern between the different agents could be observed. Contrast enhancement in a pixel in a relatively poorly perfused tumor region is depicted in Figure 5C. While only minor signal enhancement was visible, the different contrast agent boluses could still be discriminated.

Figure 6 shows representative pharmacokinetic parameter maps in the same slice shown in Figure 4. Pharmacokinetic parameters that were constrained to be identical between the different boluses are shown on the left side of the figure. In agreement with the level of contrast enhancement as shown in Figure 4, both the blood flow and blood volume were higher in the tumor rim than in the tumor center. In addition, a small region with a lack of contrast enhancement could be observed

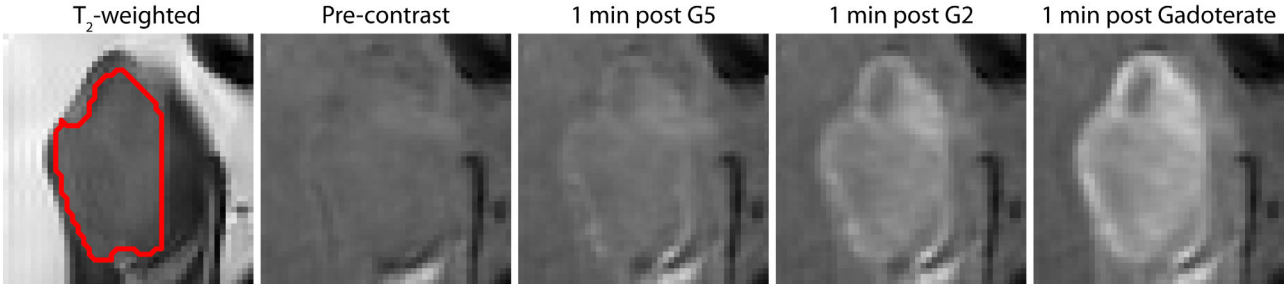


FIG. 4. Contrast enhancement in the tumor at different time points after contrast agent injection. On the left side of the figure, a $T_2$-weighted image of the tumor-bearing paw of a mouse at measurement day 1 is shown. The tumor is delineated with a red line. Peritumoral edema was not included in the ROIs. The paw is surrounded by a thin layer of ultrasound gel (light gray). DCE images of the corresponding tumor slice are shown at different time points during the dynamic acquisition. From left to right: a precontrast image, an image acquired 1 min after injection of the G5 dendrimer (1 min post G5), an image acquired 1 min after injection of the G2 dendrimer (1 min post G2), and an image acquired 1 min after injection of gadoterate (1 min post Gadoterate).

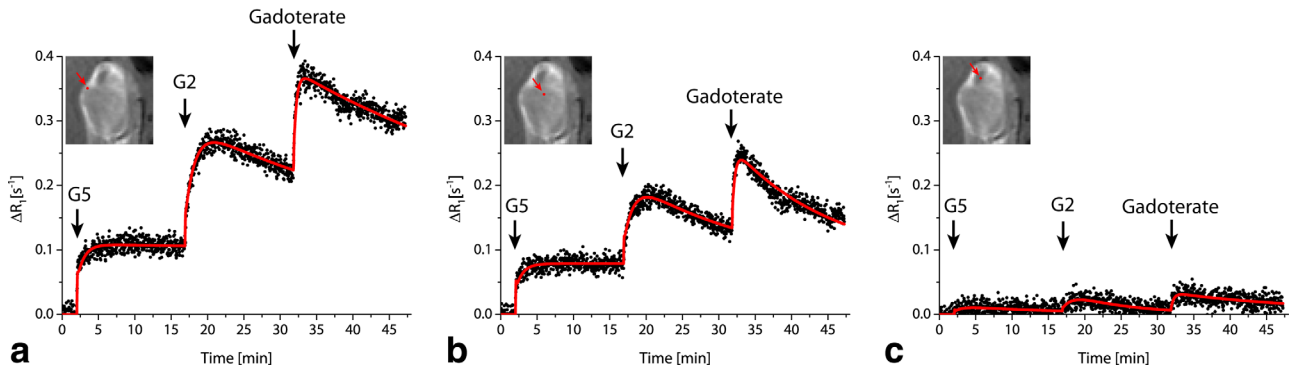


FIG. 5. Representative $\Delta R_1$ curves measured in a single tumor-pixel in the same slice as shown in Figure 4 and the multi-agent fits through the data. The location of the different pixels is indicated by red dots, overlaid on the contrast-enhanced image at 45 minutes after the first contrast agent injection. The measured data are indicated by black dots, and the multi-agent regressions are indicated by red lines. The moment of injection of the G5 and G2 dendrimer and gadoterate is indicated with black arrows. One pixel in the tumor rim (**A**), one pixel in the tumor center (**B**), and one pixel in a relatively poorly perfused region of the tumor (**C**) were selected. Estimated parameters for the pixel in the tumor rim (A) were: $F = 0.87$ min$^{-1}$, $t_c = 0.08$ min, $E(G5) = 0.20$, $k_{ep}(G5) = 0.00$ min$^{-1}$, $E(G2) = 0.34$, $k_{ep}(G2) = 0.03$ min$^{-1}$, $E(Gadoterate) = 0.85$, $k_{ep}(Gadoterate) = 0.02$ min$^{-1}$. Estimated parameters for the pixel in the tumor center (B) were: $F = 0.77$ min$^{-1}$, $t_c = 0.06$ min, $E(G5) = 0.17$, $k_{ep}(G5) = 0.00$ min$^{-1}$, $E(G2) = 0.26$, $k_{ep}(G2) = 0.06$ min$^{-1}$, $E(Gadoterate) = 0.75$, $k_{ep}(Gadoterate) = 0.07$ min$^{-1}$. Estimated parameters for the pixel in the relatively poorly perfused region (C) were: $F = 0.13$ min$^{-1}$, $t_c = 0.03$ min, $E(G5) = 0.15$, $k_{ep}(G5) = 0.06$ min$^{-1}$, $E(G2) = 0.32$, $k_{ep}(G2) = 0.13$ min$^{-1}$, $E(Gadoterate) = 1.00$, $k_{ep}(Gadoterate) = 0.04$ min$^{-1}$. Whereas F is scaled by the amplitude of the initial population-averaged AIF provided to the MCBE algorithm and absolute values of F are dependent on the global scaling factor of the AIF, relative differences in F between the curves can be directly compared. Note that if $k_{ep}$ is estimated to be equal to zero, it is not possible to provide an estimate for $v_e$. Similarly, if E is estimated to be equal to 1, PS cannot be determined.

where the blood flow and volume were low. On the right side of the figure, the contrast agent–specific pharmacokinetic parameters are displayed. In the upper panels, it can be seen that for the high molecular weight G5 dendrimer, the extraction fraction was low throughout the tumor. The medium molecular weight G2 dendrimer possessed intermediate extraction fractions, while the highest extractions were observed for the low molecular

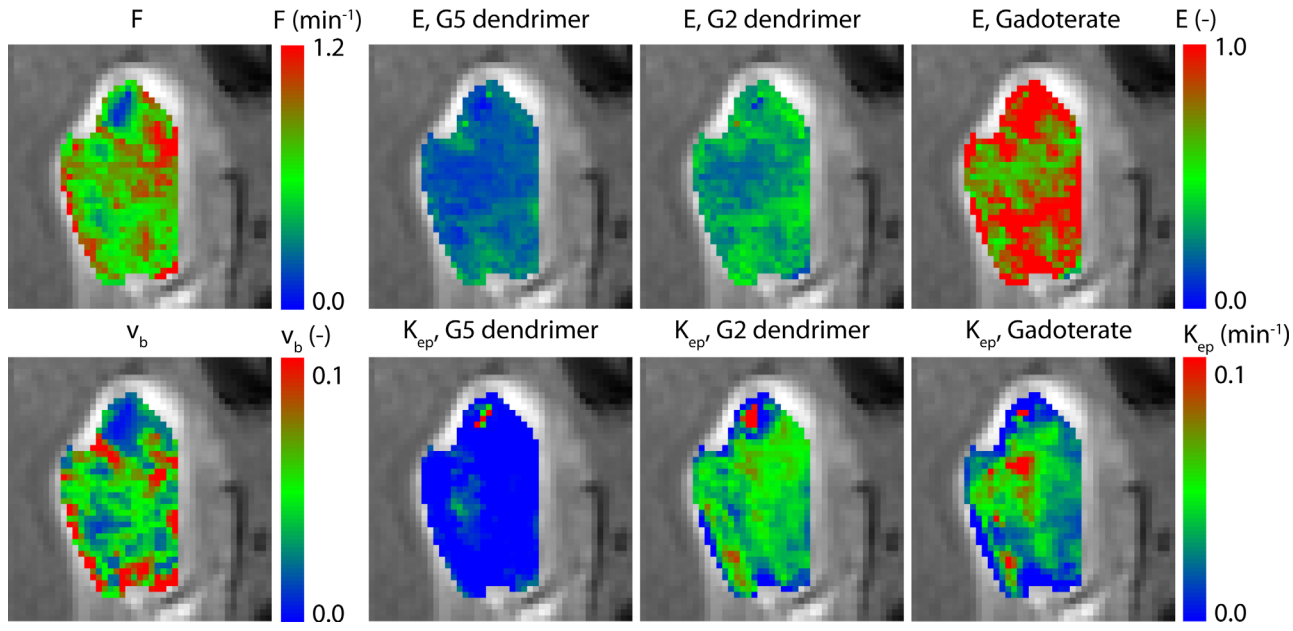


FIG. 6. Pharmacokinetic parameter maps in the same slice shown in Figure 4. The estimated pharmacokinetic parameter values are overlaid on the contrast-enhanced image at 45 min after the first contrast agent injection. Peritumoral edema (the enhancing rim) was not included in the ROIs. The plotted parameter range is indicated by the scale bars. The left-most images show pharmacokinetic parameters of the constrained parameters blood flow F (min$^{-1}$) and derived parameter fractional blood volume $v_b$ (–) in the upper and lower row, respectively. Note that F and $v_b$ are scaled by the amplitude of the initial population-averaged AIF provided to the MCBE algorithm, and the absolute values of these parameters are dependent on the global scaling factor of the AIF. The images on the right show pharmacokinetic parameter maps of the contrast agent–specific parameters extraction fraction E (–) and washout rate constant $k_{ep}$ (min$^{-1}$) in the upper and lower row, respectively.

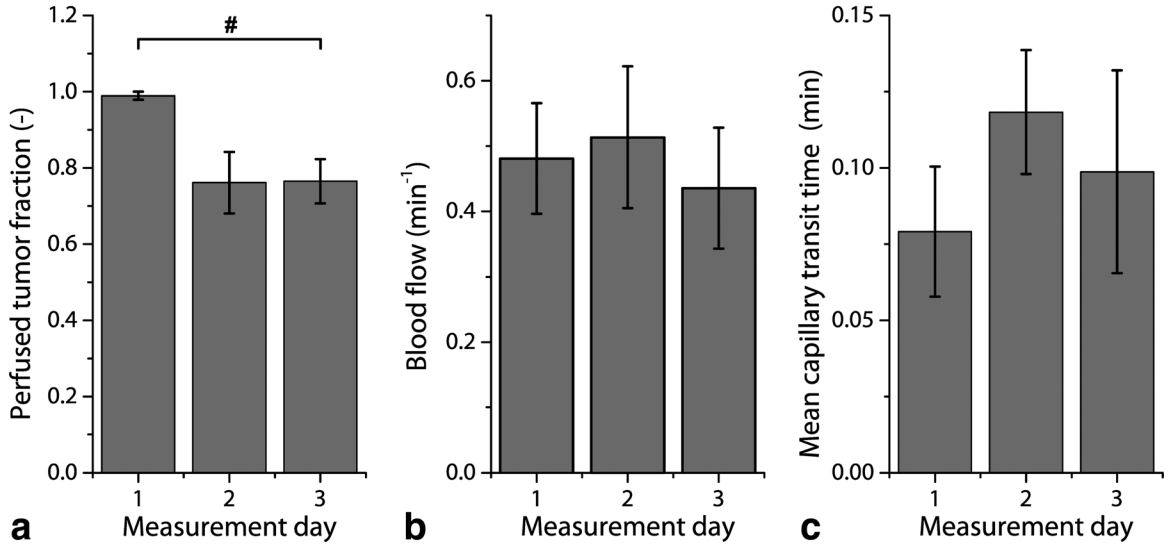


FIG. 7. Median perfused tumor fraction and constrained parameter estimates. Median ± median absolute deviation perfused tumor fraction (**A**), blood flow (**B**), and mean capillary transit time (**C**) of the five mice at the different measurement days. Whereas the blood flow is scaled by the amplitude of the initial population-averaged AIF provided to the MCBE algorithm, and its absolute value is dependent on the global scaling factor of the AIF, differences in blood flow between the measurement days can be compared directly. $^{\#}P < 0.05$ between measurement day 1 and measurement day 3.

weight gadoterate. Washout rate constants were also lowest and close to zero for the G5 dendrimer. Washout rate constants of the G2 dendrimer and gadoterate were higher, and washout rate constant maps of these contrast agents were very similar.

The median perfused tumor fraction at the different measurement days is shown in Figure 7A. At measurement day 1, nearly all of the tumor tissue was well perfused. However, a significant decrease in perfused tumor fraction was observed at measurement day 3 ($P = 0.01$). No significant differences in median tumor blood flow (Fig. 7B) or capillary transit time (Fig. 7C) in the perfused pixels were observed between the different measurement days.

The median parameter values of the contrast agent–specific pharmacokinetic parameters extraction fraction and washout rate constant are shown in Figure 8. The extraction fraction of gadoterate was consistently and significantly higher than that of both the G2 ($P = 0.002$) and G5 dendrimer ($P = 0.001$) (Fig. 8A), which was a main effect of the contrast agent on the extraction fraction. No significant difference was observed between the extraction fractions of the G2 and G5 dendrimers ($P = 0.172$), although the extraction fraction of the G2 dendrimer was

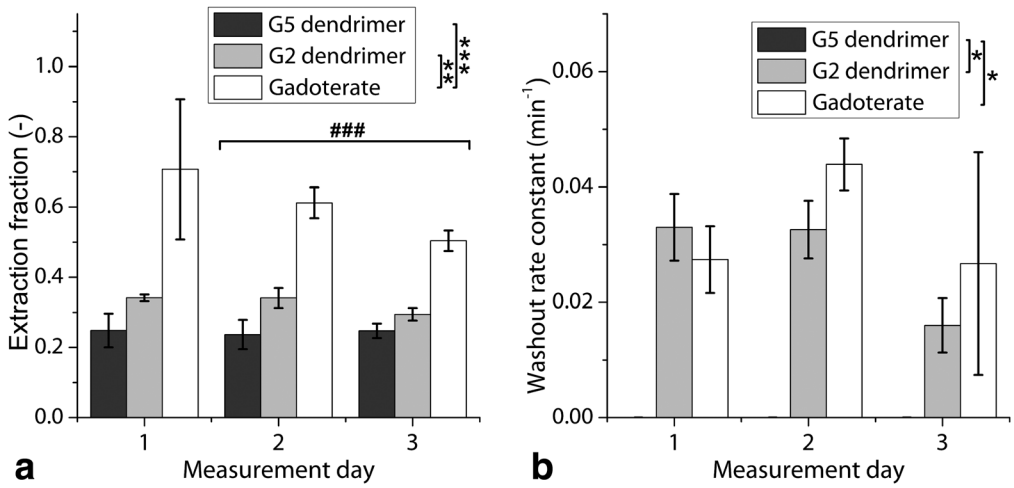


FIG. 8. Median extraction fraction and washout rate constant of the different contrast agents.The median ± median absolute deviation extraction fraction (**A**) and washout rate constant (**B**) of the five mice at the different measurement days are shown. The estimated parameter values for the G5 dendrimer, G2 dendrimer, and gadoterate are indicated by dark gray bars, light gray bars, and white bars, respectively. $^{\#\#\#}P < 0.001$ between measurement day 2 and measurement day 3. $^{*}P < 0.05$, $^{**}P < 0.01$, $^{***}P < 0.001$ between the different contrast agents.

consistently higher on all measurement days. A significant general decrease in extraction fractions was observed between measurement day 2 and 3 ($P = 0.0005$). The washout rate constants of both the G2 dendrimer ($P = 0.017$) and gadoterate ($P = 0.025$) were consistently and significantly higher than those of the G5 dendrimer, of which the rate constants were essentially zero, as would be expected for a largely intravascular agent with slow elimination kinetics. This was a main effect of the contrast agent on the washout rate constant. No significant differences were observed between the washout rate constants of the G2 dendrimer and gadoterate.

## DISCUSSION

In the present study, a novel multi-agent tracer-kinetic modeling strategy has been demonstrated, allowing blood flow and microvascular permeability to be simultaneously and self-consistently determined within one individual. The use of macromolecular contrast agents for better assessment of specific vascular biomarkers has been proposed previously, and sequential injection of multiple contrast agents has been reported. However, in these studies, injection of the different contrast agents was generally performed in separate animals or tracer-kinetic modeling was performed on the individual boluses. In the present study, constrained tracer-kinetic modeling was performed simultaneously on the multi-agent DCE-MRI data. This approach exploits the combined information of the different agents and takes advantage of the fact that a number of parameters can be constrained to be identical between the agents (based on physiological grounds) to obtain robust tracer-kinetic parameter estimates.

Monte Carlo simulations demonstrated superior accuracy and precision in determination of model parameters when using the multi-agent modeling approach relative to separate modeling of individual boluses. The better performance can be partly explained by the fact that a number of tracer-kinetic parameters were constrained to be identical between the boluses for the multi-agent approach. This will improve the modeling outcome because of the decrease in degrees of freedom in the model regressions (47). In addition, the multi-agent approach exploits the added information from measurement of uptake kinetics of contrast agents of different size. Compared with the HMW and MMW agents, the LMW agent consistently had the highest bias and uncertainty in estimated parameters, except for the estimates of $v_e$. Accurate determination of $v_e$ requires sufficient sampling of contrast agent extravasation to the interstitial space and subsequent washout. For short measurement times, both the extraction of the HMW agent into the interstitial space and subsequent washout are limited (21), which results in a high uncertainty in estimated $v_e$ values. This problem can potentially be overcome by increasing the measurement times, although undesirably long measurement times are needed to fully sample washout of the HMW agents. Nevertheless, the lowest bias and uncertainty in estimations of $v_e$ were obtained with the multi-agent approach, which further demonstrates its potential in comparison with single-bolus tracer-kinetic modeling.

The feasibility of the constrained multi-agent modeling approach was shown in vivo in a mouse tumor model. Multi-agent DCE-MRI was performed with dendrimer-based contrast agents and gadoterate, which provided a large range of molecular weights. The advantage of the dendrimers over commercially available macromolecular agents is that the size of the agents can be tuned, while the chemical composition of the agents is similar (48). Similar physiochemical properties between different agents are advantageous for multi-agent DCE-MRI, since this will minimize differences in in vivo characteristics.

Nonperfused tumor regions were excluded from tracer-kinetic analysis, since measurable blood flow is required to reliably estimate the different pharmacokinetic parameters. These nonperfused regions were assessed based on the level of signal enhancement after injection of the G5 dendrimer. Because the extraction fraction of the G5 dendrimer is low, significant signal enhancement after injection of this dendrimer is indicative of relevant blood flow in this area. Whereas contrast enhancement after injection of the G5 dendrimer was most pronounced in the highly vascular tumor rim, significant contrast enhancement could also be observed throughout the tumor (Fig. 4). Only small nonperfused fractions were observed on measurement day 1, which slightly increased on measurement day 2 and 3, likely due to natural tumor necrosis as a result of tumor growth. Therefore, multi-agent modeling could be reliably performed in the major part of the tumor.

Clear differences in contrast-enhancement in the tumor (Fig. 4) and the enhancement pattern (Fig. 5) could be observed after injection of the differently sized contrast agents. These differences in enhancement pattern translated to different tracer-kinetic parameter estimates (Fig. 8). The difference in extraction fractions between the contrast agents (Fig. 8A) shows that these agents extravasate to a different extent from the tumor vasculature into the interstitial space. Gadoterate possessed a significantly higher extraction fraction compared with the G2 and G5 dendrimers, which likely have a more intravascular distribution. This is in agreement with findings by de Lussanet et al. (21), who reported a molecular weight cutoff between 3000 and 12,000 Da, above which dendrimers possessed a mostly intravascular distribution. No significant differences were observed between the extraction fractions of the G2 and G5 dendrimers. Nevertheless, the extraction fractions of the dendrimers used in the present study were in close agreement with findings reported by Michoux et al. (49) in a rat tumor model. They assessed differences in extraction fractions of contrast agents with very similar molecular weights as used in the present study with the St Lawrence and Lee model and measured an extraction fraction of $0.51 \pm 0.17$ for gadoterate meglumine (754 Da), $0.36 \pm 0.07$ for gadomelitol (P792, Vistarem, 6470 Da), and $0.23 \pm 0.10$ for carboxymethyldextran-Gd-DOTA (P717, 52000 Da).

A significant general decrease in extraction fraction was observed from measurement day 2 to 3 (Fig. 8A). This may be due to elevated interstitial pressure, which may have resulted in decreased extravasation of contrast

agents from the tumor microvasculature (24). Elevated interstitial pressure may also lead to reduced blood flow, which is consistent with the observed decrease in perfused tumor volume on measurement day 3 compared with day 1 (Fig. 7) (50).

In addition, the washout rate constant of the G2 dendrimer and gadoterate was found to be significantly higher than that of the G5 dendrimer. The washout rate constant was essentially zero for the G5 dendrimer (Fig. 8B). As can be observed from the uptake curves in Figure 5, no clear washout could be observed for this high molecular weight agent. Therefore, washout rate constant estimates of the G5 dendrimer had a high uncertainty. This high uncertainty was also observed in the simulation results (Fig. 3). However, undesirably long acquisition times would be required to fully sample G5 dendrimer washout.

The present study has a number of limitations. The AIF was determined with the previously described MCBE algorithm, which is able to determine the AIF shape from measured tissue concentrations curves (41). Schabel et al. (42) reported good agreement between MCBE based and measured AIFs. However, the scaling of the AIF has to be performed by a secondary measurement of the blood contrast agent concentration (41). Absolute AIF scaling is known to be inherently difficult in mice. Because no animal-specific scaling of the AIF was performed in the present study, absolute pharmacokinetic parameter values could not be quantitatively compared with other studies. However, the in vivo differences in extraction fraction and rate constant between the different agents are consistent regardless of the bolus profile and AIF scaling, which would only affect absolute estimates of F and $v_b$ (16). Increasing the temporal resolution of the dynamic acquisition and optimizing the flip angle to be optimally sensitive to the expected range of contrast agent concentrations in the plasma compartment and interstitial space might further improve measurement accuracy and AIF extraction by the MCBE algorithm (40).

The multi-agent modeling approach uses the fact that a number of parameters can be constrained to be identical between the agents to obtain robust tracer-kinetic parameter estimates. Whereas this may be generally valid, it has been reported that tumors could display intermittent blood flow that can occur rapidly in independent single blood vessels, or regionally at cyclic time intervals (in the order of 15 min to over 1 h) (51–56). It is expected that blood flow fluctuations in single vessels have a minor effect in their contribution to the whole voxel signal intensity. High-frequency fluctuations (on time scales of seconds) will be mostly averaged out considering the 1.89 s acquisition time. However, regional blood flow fluctuations occurring at longer time scales could possibly be of influence on tracer-kinetic parameter estimations. However, in the vast majority of cases, the multi-agent modeling was able to fit all three boluses with a single flow value. If the voxel level flow values would vary strongly between the different boluses, good multi-agent model fits could not be obtained, and the accuracy in the estimated blood flow would be low. Because voxels with low blood flow fitting accuracy were excluded from further analysis, this limits the effect of strong blood flow fluctuations on the results. Nevertheless, in future studies, the total multi-agent acquisition time could be reduced to approximately 10 min in order to ensure that the constrained parameters are more constant during the DCE-MRI acquisition.

Extensive validation of the estimated tracer-kinetic parameters was beyond the scope of this study. Multi-agent blood flow estimations could be validated with ultrahigh sensitive optical microangiography, which is a label-free optical imaging method that is able to measure microcirculatory blood flow via endogenous backscattered light from flowing red blood cells (57). The mean capillary transit times could be validated with in vivo two-photon laser microscopy measurements of fluorescently labeled dextrans of comparable molecular weight (58), or alternatively the contrast agents that were used in the multi-agent approach could be fluorescently labeled and tracked in vivo to assess the dynamics of the passing bolus in the tumor. In addition, this technique could be employed to assess differences in the extent of extravasation of the different contrast agents (58,59).

## CONCLUSION

We have demonstrated a novel approach to tracer-kinetic modeling of macromolecular DCE-MRI data. Simulations showed that constrained multi-agent model regressions led to less uncertainty and bias in estimated tracer-kinetic parameters in comparison with single-bolus modeling. The approach was successfully applied in vivo in a mouse tumor model and significant differences in extraction fraction, and washout rate constant between the different agents, dependent on their molecular weight, were consistently observed on the different measurement days. The in vivo results indicated that tumor blood flow could be separately determined from contrast agent–specific permeability and washout-related tracer-kinetic parameters. It is expected that the multi-agent modeling approach can be applied to accurately evaluate treatment effects on different vascular biomarkers. In addition, by assessment of the differential leakage of the contrast agents of various molecular weight, the method may be able to predict the efficacy of nanomedicine delivery to the tumor (60).

## REFERENCES

1. Eichhorn ME, Strieth S, Dellian M. Anti-vascular tumor therapy: recent advances, pitfalls and clinical perspectives. Drug Resist Updat 2004;7:125–138.
2. Jackson A. Imaging microvascular structure with contrast enhanced MRI. Br J Radiol 2003;76:S159–S173.
3. Padhani AR, Leach MO. Antivascular cancer treatments: functional assessments by dynamic contrast-enhanced magnetic resonance imaging. Abdom Imaging 2005;30:324–341.
4. Zweifel M, Padhani AR. Perfusion MRI in the early clinical development of antivascular drugs: decorations or decision making tools? Eur J Nucl Med Mol Imaging 2010;37(Suppl 1):S164–S182.
5. O'Connor JP, Jackson A, Parker GJ, Roberts C, Jayson GC. Dynamic contrast-enhanced MRI in clinical trials of antivascular therapies. Nat Rev Clin Oncol 2012;9:167–177.
6. O'Connor JP, Jackson A, Parker GJ, Jayson GC. DCE-MRI biomarkers in the clinical evaluation of antiangiogenic and vascular disrupting agents. Br J Cancer 2007;96:189–195.

7. O'Connor JP, Jackson A, Asselin MC, Buckley DL, Parker GJ, Jayson GC. Quantitative imaging biomarkers in the clinical development of targeted therapeutics: current and future perspectives. Lancet Oncol 2008;9:766–776.
8. Koh TS, Thng CH, Hartono S, et al. A comparative study of dynamic contrast-enhanced MRI parameters as biomarkers for anti-angiogenic drug therapy. NMR Biomed 2011;24:1169–1180.
9. Tofts PS, Kermode AG. Measurement of the blood-brain barrier permeability and leakage space using dynamic MR imaging. 1. Fundamental concepts. Magn Reson Med 1991;17:357–367.
10. Tofts PS, Brix G, Buckley DL, et al. Estimating kinetic parameters from dynamic contrast-enhanced T1-weighted MRI of a diffusable tracer: standardized quantities and symbols. J Magn Reson Imaging 1999;10:223–232.
11. Sourbron SP, Buckley DL. On the scope and interpretation of the Tofts models for DCE-MRI. Magn Reson Med 2011;66:735–745.
12. Tozer GM, Prise VE, Wilson J, Cemazar M, Shan S, Dewhirst MW, Barber PR, Vojnovic B, Chaplin DJ. Mechanisms associated with tumor vascular shut-down induced by combretastatin A-4 phosphate: intravital microscopy and measurement of vascular permeability. Cancer Res 2001;61:6413–6422.
13. Tozer GM, Kanthou C, Parkins CS, Hill SA. The biology of the combretastatins as tumour vascular targeting agents. Int J Exp Pathol 2002;83:21–38.
14. Carmeliet P, Jain RK. Principles and mechanisms of vessel normalization for cancer and other angiogenic diseases. Nat Rev Drug Discov 2011;10:417–427.
15. Jain RK. Normalization of tumor vasculature: an emerging concept in antiangiogenic therapy. Science 2005;307:58–62.
16. Sourbron SP, Buckley DL. Classic models for dynamic contrast-enhanced MRI. NMR Biomed 2013;26:1004–1027.
17. Sourbron SP, Buckley DL. Tracer kinetic modelling in MRI: estimating perfusion and capillary permeability. Phys Med Biol 2012;57:R1–R33.
18. Larsson HB, Courivaud F, Rostrup E, Hansen AE. Measurement of brain perfusion, blood volume, and blood-brain barrier permeability, using dynamic contrast-enhanced T1-weighted MRI at 3 Tesla. Magn Reson Med 2009;62:1270–1281.
19. Lopata RG, Backes WH, van den Bosch PP, van Riel NA. On the identifiability of pharmacokinetic parameters in dynamic contrast-enhanced imaging. Magn Reson Med 2007;58:425–429.
20. Sourbron S. Technical aspects of MR perfusion. Eur J Radiol 2010;76:304–313.
21. de Lussanet QG, Langereis S, Beets-Tan RG, van Genderen MH, Griffioen AW, van Engelshoven JM, Backes WH. Dynamic contrast-enhanced MR imaging kinetic parameters and molecular weight of dendritic contrast agents in tumor angiogenesis in mice. Radiology 2005;235:65–72.
22. Jaspers K, Aerts HJ, Leiner T, Oostendorp M, van Riel NA, Post MJ, Backes WH. Reliability of pharmacokinetic parameters: small vs. medium-sized contrast agents. Magn Reson Med 2009;62:779–787.
23. Fruytier AC, Magat J, Neveu MA, Karroum O, Bouzin C, Feron O, Jordan B, Cron GO, Gallez B. Dynamic contrast-enhanced MRI in mouse tumors at 11.7 T: comparison of three contrast agents with different molecular weights to assess the early effects of combretastatin A4. NMR Biomed 2014;27:1403–1412.
24. Hompland T, Gulliksrud K, Ellingsen C, Rofstad EK. Assessment of the interstitial fluid pressure of tumors by dynamic contrast-enhanced magnetic resonance imaging with contrast agents of different molecular weights. Acta Oncol 2013;52:627–635.
25. Weidensteiner C, Rausch M, McSheehy PM, Allegrini PR. Quantitative dynamic contrast-enhanced MRI in tumor-bearing rats and mice with inversion recovery TrueFISP and two contrast agents at 4.7 T. J Magn Reson Imaging 2006;24:646–656.
26. Delrue LJ, Casneuf V, Van Damme N, Blanckaert P, Peeters M, Ceelen WP, Duyck PC. Assessment of neovascular permeability in a pancreatic tumor model using dynamic contrast-enhanced (DCE) MRI with contrast agents of different molecular weights. MAGMA 2011;24:225–232.
27. Ivanusa T, Beravs K, Medic J, Sersa I, Sersa G, Jevtic V, Demsar F, Mikac U. Dynamic contrast enhanced MRI of mouse fibrosarcoma using small-molecular and novel macromolecular contrast agents. Phys Med 2007;23:85–90.
28. Preda A, Novikov V, Moglich M, Turetschek K, Shames DM, Brasch RC, Cavagna FM, Roberts TP. MRI monitoring of Avastin antiangiogenesis therapy using B22956/1, a new blood pool contrast agent, in an experimental model of human cancer. J Magn Reson Imaging 2004;20:865–873.
29. Beaumont M, Lemasson B, Farion R, Segebarth C, Remy C, Barbier EL. Characterization of tumor angiogenesis in rat brain using iron-based vessel size index MRI in combination with gadolinium-based dynamic contrast-enhanced MRI. J Cereb Blood Flow Metab 2009;29:1714–1726.
30. Pike MM, Stoops CN, Langford CP, Akella NS, Nabors LB, Gillespie GY. High-resolution longitudinal assessment of flow and permeability in mouse glioma vasculature: sequential small molecule and SPIO dynamic contrast agent MRI. Magn Reson Med 2009;61:615–625.
31. Orth RC, Bankson J, Price R, Jackson EF. Comparison of single- and dual-tracer pharmacokinetic modeling of dynamic contrast-enhanced MRI data using low, medium, and high molecular weight contrast agents. Magn Reson Med 2007;58:705–716.
32. Henderson E, Sykes J, Drost D, Weinmann HJ, Rutt BK, Lee TY. Simultaneous MRI measurement of blood flow, blood volume, and capillary permeability in mammary tumors using two different contrast agents. J Magn Reson Imaging 2000;12:991–1003.
33. Su MY, Muhler A, Lao XY, Nalcioglu O. Tumor characterization with dynamic contrast-enhanced MRI using MR contrast agents of various molecular weights. Magn Reson Med 1998;39:259–269.
34. Jacobs I, Strijkers GJ, Keizer HM, Janssen HM, Nicolay K, Schabel MC. A novel approach to tracer-kinetic modeling of (macromolecular) multi-bolus DCE-MRI data, applied in a murine tumor model. In Proceedings of the 22nd Annual Meeting of ISMRM, Milan, Italy, 2014. Abstract 42.
35. Schabel MC. A unified impulse response model for DCE-MRI. Magn Reson Med 2012;68:1632–1646.
36. Renkin EM. Transport of potassium-42 from blood to tissue in isolated mammalian skeletal muscles. Am J Physiol 1959;197:1205–1210.
37. Crone C. The permeability of capillaries in various organs as determined by use of the 'indicator diffusion' method. Acta Physiol Scand 1963;58:292–305.
38. Jensen RL, Mumert ML, Gillespie DL, Kinney AY, Schabel MC, Salzman KL. Preoperative dynamic contrast-enhanced MRI correlates with molecular markers of hypoxia and vascularity in specific areas of intratumoral microenvironment and is predictive of patient outcome. Neuro Oncol 2014;16:280–291.
39. Deoni SC, Rutt BK, Peters TM. Rapid combined T1 and T2 mapping using gradient recalled acquisition in the steady state. Magn Reson Med 2003;49:515–526.
40. Schabel MC, Parker DL. Uncertainty and bias in contrast concentration measurements using spoiled gradient echo pulse sequences. Phys Med Biol 2008;53:2345–2373.
41. Schabel MC, Fluckiger JU, DiBella EV. A model-constrained Monte Carlo method for blind arterial input function estimation in dynamic contrast-enhanced MRI: I. Simulations. Phys Med Biol 2010;55:4783–4806.
42. Schabel MC, DiBella EV, Jensen RL, Salzman KL. A model-constrained Monte Carlo method for blind arterial input function estimation in dynamic contrast-enhanced MRI: II. In vivo results. Phys Med Biol 2010;55:4807–4823.
43. Dowell NG, Tofts PS. Fast, accurate, and precise mapping of the RF field in vivo using the 180 degrees signal null. Magn Reson Med 2007;58:622–630.
44. Liberman G, Louzoun Y, Ben Bashat D. T1 mapping using variable flip angle SPGR data with flip angle correction. J Magn Reson Imaging 2014;40:171–180.
45. Yarnykh VL. Optimal radiofrequency and gradient spoiling for improved accuracy of T1 and B1 measurements using fast steady-state techniques. Magn Reson Med 2010;63:1610–1626.
46. van Nierop BJ, Coolen BF, Dijk WJ, Hendriks AD, de Graaf L, Nicolay K, Strijkers GJ. Quantitative first-pass perfusion MRI of the mouse myocardium. Magn Reson Med 2013;69:1735–1744.
47. Kershaw LE, Cheng HL. Temporal resolution and SNR requirements for accurate DCE-MRI data analysis using the AATH model. Magn Reson Med 2010;64:1772–1780.
48. Langereis S, de Lussanet QG, van Genderen MH, Meijer EW, Beets-Tan RG, Griffioen AW, van Engelshoven JM, Backes WH. Evaluation of Gd(III)DTPA-terminated poly(propylene imine) dendrimers as contrast agents for MR imaging. NMR Biomed 2006;19:133–141.
49. Michoux N, Huwart L, Abarca-Quinones J, Dorvillius M, Annet L, Peeters F, Van Beers BE. Transvascular and interstitial transport in rat hepatocellular carcinomas: dynamic contrast-enhanced MRI assessment with low- and high-molecular weight agents. J Magn Reson Imaging 2008;28:906–914.

50. Milosevic MF, Fyles AW, Hill RP. The relationship between elevated interstitial fluid pressure and blood flow in tumors: a bioengineering analysis. Int J Radiat Oncol 1999;43:1111–1123.
51. Chaplin DJ, Hill SA. Temporal heterogeneity in microregional erythrocyte flux in experimental solid tumours. Br J Cancer 1995;71:1210–1213.
52. Dewhirst MW, Kimura H, Rehmus SW, Braun RD, Papahadjopoulos D, Hong K, Secomb TW. Microvascular studies on the origins of perfusion-limited hypoxia. Br J Cancer Suppl 1996;27:S247–S251.
53. Kimura H, Braun RD, Ong ET, Hsu R, Secomb TW, Papahadjopoulos D, Hong K, Dewhirst MW. Fluctuations in red cell flux in tumor microvessels can lead to transient hypoxia and reoxygenation in tumor parenchyma. Cancer Res 1996;56:5522–5528.
54. Baudelet C, Ansiaux R, Jordan BF, Havaux X, Macq B, Gallez B. Physiological noise in murine solid tumours using T2*-weighted gradient-echo imaging: a marker of tumour acute hypoxia? Phys Med Biol 2004;49:3389–3411.
55. Brurberg KG, Benjaminsen IC, Dorum LM, Rofstad EK. Fluctuations in tumor blood perfusion assessed by dynamic contrast-enhanced MRI. Magn Reson Med 2007;58:473–481.
56. Brurberg KG, Gaustad JV, Mollatt CS, Rofstad EK. Temporal heterogeneity in blood supply in human tumor xenografts. Neoplasia 2008;10:727–735.
57. Jia Y, Qin J, Zhi Z, Wang RK. Ultrahigh sensitive optical microangiography reveals depth-resolved microcirculation and its longitudinal response to prolonged ischemic event within skeletal muscles in mice. J Biomed Opt 2011;16:086004.
58. Bragin DE, Bush RC, Nemoto EM. Effect of cerebral perfusion pressure on cerebral cortical microvascular shunting at high intracranial pressure in rats. Stroke 2013;44:177–181.
59. Dreher MR, Liu W, Michelich CR, Dewhirst MW, Yuan F, Chilkoti A. Tumor vascular permeability, accumulation, and penetration of macromolecular drug carriers. J Natl Cancer Inst 2006;98:335–344.
60. Chauhan VP, Stylianopoulos T, Martin JD, Popovic Z, Chen O, Kamoun WS, Bawendi MG, Fukumura D, Jain RK. Normalization of tumour blood vessels improves the delivery of nanomedicines in a size-dependent manner. Nat Nanotechnol 2012;7:383–388.
61. Corot C, Port M, Raynal I, et al. Physical, chemical, and biological evaluations of P760: a new gadolinium complex characterized by a low rate of interstitial diffusion. J Magn Reson Imaging 2000;11:182–191.

## SUPPORTING INFORMATION

Additional Supporting Information may be found in the online version of this article.

**Supporting Figure 1.1.** Synthesis scheme. Synthesis of G2-PPI-$(PEG_6$-$GdDOTA)_8$ and G5-PPI-$(PEG_6$-$GdDOTA)_{64}$. The building block with a discrete number of ethylene glycol units 1 was synthesized according to literature procedure.[1–3] a) PyBOP, DiPEA, DCM; b) TFA, DCM; c) DOTA-NHS, TEA, MeOH; d) $Gd(OAc)_3$, $H_2O$, pH$\sim$7.

**Supporting Figure 1.2.** Dynamic light scattering results. The volume-weighted size (hydrodynamic diameter) distribution of the G2 and G5 dendrimer, measured in PBS of pH 7.4 at 20°C.

**Supporting Figure 2.1.** Phantom validation of the variable flip angle $T_1$ mapping method. Correlation plot between the variable flip angle $R_1$ ($s^{-1}$) and the inversion recovery $R_1$ ($s^{-1}$) of samples containing various concentrations (0.05–1.5 mM) of gadoterate in 5 mg/L manganese(II) chloride. The red line is the linear fit to the data, with the equation and $R^2$ of the linear fit displayed in the graph.

**Supporting Figure 2.2.** Phantom validation of the dynamic $T_1$ mapping method. Correlation plot between the dynamic $R_1$ ($s^{-1}$) and the inversion recovery $R_1$ ($s^{-1}$) of samples containing various concentrations (0.05–1.5 mM) of gadoterate in 5 mg/L manganese(II) chloride. The red line is the linear fit to the data, with the equation and $R^2$ of the linear fit displayed in the graph.

**Supporting Figure 3.1.** Typical AIFs of the dendrimers and gadoterate, as determined with the MCBE algorithm. The time scale on the x-axis refers to the time after start of the acquisition.